

Ultralight Dark Matter Detection with a Ferromagnet Lattice

Dongyi Yang,¹ Xiao Yang,² Chenxi Sun,^{2,*} and Jianwei Zhang^{1,†}

¹*School of Physics, Peking University, Beijing 100871, China*

²*Beijing Key Laboratory of Quantum Sensing and Precision Measurement,
and Center for Quantum Information Technology,
and Institute of Quantum Electronics, Peking University, Beijing 100871, China*

(Dated: February 20, 2026)

A levitated ferromagnet provides an exceptionally sensitive probe of ultralight dark matter (ULDM) through measuring weak magnetic-like field signals. We propose a ferromagnet lattice magnetometer that coherently combines multiple levitated ferromagnets to enhance effective sensitivity. By replacing a single ferromagnet with a lattice, we increase the total polarized spin while preserving the intrinsic dynamical response of each constituent ferromagnet. We show that magnetic dipole-dipole interactions within the lattice can be dynamically suppressed through a high-frequency magnetic field, rendering the system effectively noninteracting, at the cost of only a moderate reduction in signal amplitude due to the distinct renormalization of linear and quadratic spin responses. We analyze the noise properties of the lattice and demonstrate that collective readout leads to favorable scaling with the number of ferromagnets. Interpreted in terms of axion-electron, dark photon, and axion-photon couplings, our results yield projected sensitivities that significantly exceed existing single-ferromagnet implementations. In particular, for axion-photon interactions, we find a nontrivial lattice-induced enhancement of the signal itself, leading to sensitivities that surpass existing constraints over a broad mass range.

Ultralight dark matter (ULDM) is a class of well-motivated dark matter models described by a scalar particle, whose extremely small mass allows it to behave as a coherently oscillating classical field on laboratory timescales [1, 2]. Through its couplings to standard model particles, ULDM induces spin-dependent interactions that can be described as weak, narrowband, and low-frequency magnetic-like fields, making high-precision magnetometry well-suited for its detection [3, 4]. In this context, spin-based magnetometers with long coherence times are especially powerful, and have enabled a broad experimental program targeting axions, dark photons, and related candidates [5, 6].

Among various magnetometric platforms, levitated ferromagnets offer a distinctive combination of large intrinsic spin polarization, low mechanical dissipation, and long coherence times [7, 8]. The macroscopic magnetic moment of a single ferromagnet enables coherent rotational dynamics in response to extremely weak magnetic fields, which can be read out with high precision using a superconducting quantum interference device (SQUID). Importantly, levitation isolates the ferromagnet from environmental mechanical noise, allowing its spin dynamics to operate close to fundamental limits. These features make levitated ferromagnets a particularly suitable platform for ULDM searches in the low-frequency regime. A natural strategy to further enhance the detection capability is to increase the total number of polarized spins participating in the measurement. For a single ferromagnet, this can be attempted by enlarging its size. However, practical constraints on levitation and the rapid growth of the moment of inertia limit this approach and degrade the high-frequency response [9].

In this letter, we instead propose a qualitatively dif-

ferent route by replacing a single levitated ferromagnet with a lattice of N identical ferromagnets. The lattice increases the total polarized spin and enables a collective readout that improves the effective sensitivity to ULDM-induced magnetic-like fields. While inter-particle magnetic dipole-dipole interactions generically lead to rapid dephasing and would destroy the collective response, we show that this challenge can be overcome by applying a high-frequency magnetic field that dynamically suppresses the transverse dipolar interactions, rendering the lattice effectively non-interacting on magnetometry timescales. As a result, the lattice preserves single-ferromagnet dynamics while achieving a strong enhancement in effective signal-to-noise ratio (SNR).

Beyond this general enhancement, the ferromagnet lattice exhibits a particularly distinctive advantage in the axion-photon coupling channel. Unlike axion-electron or dark-photon interactions, where the ULDM-induced magnetic-like field is determined solely by the dark matter background, the axion-photon signal depends linearly on the ambient electromagnetic field. In our setup, this background field is generated collectively by the ferromagnet lattice itself, leading to an additional enhancement of the effective signal that scales with the number of ferromagnets. This nontrivial interplay places the lattice in a qualitatively different regime for axion-photon searches, enabling sensitivities that surpass existing constraints.

The dynamics of a single levitated ferromagnetic particle are described by its total angular momentum $\mathbf{J} = \mathbf{L} + \mathbf{S}$ and the orientation of its intrinsic spin, $\hat{\mathbf{n}} = \mathbf{S}/|\mathbf{S}|$. In the presence of an external potential V , the equations

of motion read

$$\partial_t \mathbf{J} = -\hat{\mathbf{n}} \times \nabla_{\hat{\mathbf{n}}} V, \quad \partial_t \hat{\mathbf{n}} = \boldsymbol{\Omega} \times \hat{\mathbf{n}}, \quad (1)$$

where $\boldsymbol{\Omega}$ is the angular velocity and $\mathbf{L} = I\boldsymbol{\Omega}$ defines the moment of inertia I . For small angular deviations about an equilibrium orientation (θ_0, ϕ_0) , the equations of motion can be linearized and expressed in terms of angular fluctuations $(\delta\theta, \delta\phi)$. The resulting dynamics are characterized by a susceptibility matrix $\chi(\omega)$, which relates an applied oscillating magnetic field to the angular response of the ferromagnet. When exposed to a weak alternating-current (ac) magnetic field $\mathbf{B}(t) = \mathbf{B}_0 \cos \omega t$, the response takes the form [8]

$$\begin{pmatrix} \delta\theta \\ \delta\phi \end{pmatrix} = -\mu B_0 \chi(\omega) \begin{pmatrix} b_\theta \\ b_\phi \end{pmatrix}, \quad (2)$$

where μ is the magnetic moment of the ferromagnet and (b_θ, b_ϕ) specifies the direction of the magnetic field.

The susceptibility matrix encodes oscillatory motions in its diagonal elements and precessional motions in its off-diagonal elements. In the operating regime relevant for magnetometry, the trapping potential is sufficiently strong to dominate the motion of the ferromagnet by oscillations. The detailed form of $\chi(\omega)$ and the derivation of the linearized equations of motion can be found in ref. [8], and for our purposes, its simplified expression is

$$\chi(\omega)^{-1} = I \left[-\omega^2 \begin{pmatrix} 1 & 0 \\ 0 & 1 \end{pmatrix} + \omega_I \begin{pmatrix} v_{\theta\theta} & 0 \\ 0 & v_{\phi\phi} \end{pmatrix} \right], \quad (3)$$

where $\omega_I = \mu/\gamma_e I$ is the Einstein-de Haas frequency, γ_e is the electron gyromagnetic ratio, and $v_{ij} = (\gamma_e/\mu) \partial_i \partial_j V$, with $i, j = \theta, \phi$.

We now generalize the single-ferromagnet description to a lattice consisting of N identical ferromagnets. The ferromagnets are aligned at fixed positions \mathbf{r}_i , forming a stationary crystal-like lattice configuration. The levitation and spatial separation of multiple ferromagnets could be realized using acoustic standing-wave fields or ultrasonic phased-array techniques, which are capable of generating multiple stable trapping sites and lattice-like configurations for suspended particles [10–12]. An alternative approach is through optical levitation [13]. Superconducting levitation strongly restricts the vertical extension of the lattice and is thus unfavorable for the lattice configuration.

When extending levitated ferromagnet magnetometry from a single particle to a lattice, magnetic dipole–dipole interactions naturally emerge as the dominant many-body effect. Each ferromagnet generates a magnetic field that acts back on its neighbors, producing a spatially inhomogeneous and time-dependent magnetic-like environment within the lattice. The primary consequence of such interactions is dephasing. Although all particles can be initialized in the same magnetization state, this

configuration corresponds to an equilibrium point of the dipole–dipole interaction rather than a stationary one. Because the interaction between macroscopic magnetic dipoles energetically favors anti-alignment, small environmental perturbations drive the system away from this equilibrium, leading to a gradual loss of phase coherence in the transverse magnetization and suppressing the collective signal that would otherwise scale constructively with particle number.

Importantly, not all components of the dipole–dipole interaction contribute equally to this dephasing process. Longitudinal interactions, aligned with the mean magnetization direction, primarily induce static frequency shifts and do not by themselves lead to coherence loss. In contrast, transverse interaction components generate torques that directly scramble the relative phases between different particles, making them the dominant source of dephasing in the lattice. To suppress this effect, we apply a high-frequency oscillating magnetic field that is spatially uniform across the lattice. Such a drive modulates the ferromagnet dynamics by a high-frequency oscillation, so that on the longer timescales relevant for magnetometry, the residual dynamics is governed by an effective time-averaged interaction. The time-averaged dipole–dipole interaction takes the form

$$H_{ij} = \frac{\mu_0 \mu^2}{4\pi r_{ij}^3} \left[n_i^z n_j^z - \frac{1}{2} J_0(2\alpha) \mathbf{n}_i^\perp \cdot \mathbf{n}_j^\perp \right] (1 - 3(\hat{r}_{ij})_z^2), \quad (4)$$

where z denotes the equilibrium magnetization direction, $i, j = 1, \dots, N$ denotes the indices of the ferromagnets, and \perp the transverse plane. The high-frequency drive renormalizes the transverse component of the interaction by a Bessel-function factor, while leaving the longitudinal component unchanged. At the first zero of $J_0(2\alpha)$, the leading-order transverse dipole–dipole interaction is completely suppressed.

The dynamical averaging does not renormalize the signal and the dipole–dipole interaction in the same way. The response to an external magnetic field depends linearly on the magnetization direction $\mathbf{n}(t)$, whereas the dipole–dipole interaction is quadratic in $\mathbf{n}(t)$. As a result, averaging over the fast drive suppresses the interaction more strongly than the signal. After averaging, the signal response acquires an additional factor of $J_0(\alpha)$, while the transverse dipole–dipole interaction is renormalized by $J_0(2\alpha)$. This separation of scaling allows one to choose the driving field such that dephasing is dynamically suppressed while a substantial signal response is retained. Consequently, the driven lattice can be rendered effectively non-interacting on magnetometry timescales, while preserving coherent signal accumulation across the array.

The magnetic-field noise of the ferromagnet lattice can be decomposed into three contributions [14],

$$S_B = S_B^{\text{th}} + S_B^{\text{imp}} + S_B^{\text{back}}, \quad (5)$$

where S_B denotes the power spectral density. The corresponding single-ferromagnet contributions have been analyzed in detail in ref. [8]; here we focus on their scaling with the number of ferromagnets N . The three terms exhibit distinct N -dependence. Thermal fluctuations S_B^{th} , arising from independent environmental perturbations on each particle, are reduced by $1/N$ under collective readout. In contrast, the backaction term S_B^{back} , originating from SQUID current fluctuations, is fully correlated across the lattice and therefore independent of N . The imprecision term S_B^{imp} is associated with flux readout fluctuations. Since the collective signal scales linearly with N , the equivalent magnetic-field fluctuation is suppressed as $1/N^2$. Including the dynamical renormalization of the magnetic susceptibility by a factor $J_0(\alpha_0)$, the total noise spectrum becomes

$$S_B = \frac{1}{N} S_{B,1}^{\text{th}} + S_{B,1}^{\text{back}} + \frac{1}{N^2 J_0^2(\alpha_0)} S_{B,1}^{\text{imp}}. \quad (6)$$

Because backaction originates in the SQUID circuitry rather than in the ferromagnet response, it is unaffected by the dynamical renormalization.

Although the backaction term is not reduced by increasing N , its impact on the total noise can be mitigated through noise rebalancing in the readout. In practice, the magnetic flux from the ferromagnet lattice is collected by a pickup coil and coupled to the SQUID via an effective coupling constant η . Backaction noise scales as η^2 , while imprecision noise scales as η^{-2} , allowing their relative contributions to be tuned by adjusting the pickup-coil configuration [8]. Because the imprecision term is suppressed most efficiently by collective operation, it can be partially sacrificed to rebalance the backaction term, such that both contributions can be tuned to be parametrically comparable to the thermal noise floor. The frequency dependence of the total noise spectrum of a typical parameter setup is shown in FIG. 1.

Other possible noise sources include residual effects of dipole–dipole interactions and small variations in ferromagnet properties across the lattice. As discussed earlier, dipole–dipole interactions are dynamically suppressed on magnetometry timescales and contribute only weak, effectively stochastic torques, whose noise scales in the same manner as thermal noise and can be made negligible through appropriate choice of the driving parameters. Fabrication-induced variations lead to mild changes in the shape of susceptibility without introducing additional noise channels. As a result, these factors do not constitute a fundamental limitation of the lattice performance.

In the following, we interpret the magnetic-field sensitivity of the proposed ferromagnet lattice magnetometer in the context of ULDM searches. We consider several well-motivated scenarios where ULDM manifests as a coherently oscillating classical field, inducing an effective oscillatory magnetic field in the laboratory. The

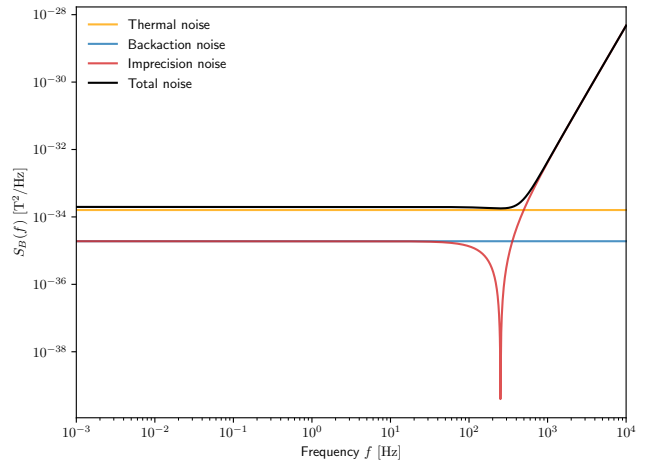


FIG. 1. Magnetic-field noise power spectral density $S_B(f)$ for the ferromagnet lattice. The total spectrum (black) is shown together with its dominant contributions: thermal, backaction, and imprecision components. The imprecision term is computed using the frequency-dependent susceptibility $\chi(\omega)$ in Eq. (3), leading to a pronounced rise at high frequencies. For $v_{\phi\theta} = v_{\phi\phi}$, the system exhibits a single resonance frequency. The low-frequency regime is thermally limited, whereas at higher frequencies the imprecision term determines the sensitivity. Frequencies above 10 kHz are not considered reliable due to overlap with the high-frequency modulation.

absence of an experimentally observable signal could allow us to place constraints on the corresponding coupling strengths. We assume a local dark matter energy density ρ_{DM} and that the dark matter field oscillates at its Compton frequency $\omega_{\text{DM}} = m_{\text{DM}}$, using natural units where $\hbar = c = \mu_0 = 1$ [1]. The bandwidth of the effective magnetic field is given by its energy dispersion as $\delta f_{\text{DM}} \equiv 1/t_{\text{cor}} \sim v_{\text{DM}}^2 \omega_{\text{DM}}/2\pi$, resulting in a signal-to-noise ratio (SNR) of [8]

$$\text{SNR} = \frac{B_{\text{DM}}^2}{6} \sqrt{\text{Tr} \left[(S^{\text{tot}})^{-2} \right] \cdot t_{\text{int}} \cdot \min(t_{\text{int}}, t_{\text{coh}})}, \quad (7)$$

where $t_{\text{int}} = 1$ year is the integration time. A criterion of $\text{SNR} \leq 3$ is assumed to set the upper limit.

We first consider an axion-like particle a coupled to electrons through its derivative

$$\mathcal{L}_{\text{ae}} = \frac{g_{\text{ae}}}{2m_e} \partial_\mu a \bar{\psi}_e \gamma^\mu \gamma^5 \psi_e, \quad (8)$$

which induces a coupling between the axion field gradient and the electron spin. In the nonrelativistic limit, the axion interaction leads to an effective magnetic field given by

$$\mathbf{B}_{\text{ae}} = \frac{g_{\text{ae}}}{\gamma_e m_e} \nabla a. \quad (9)$$

For axion dark matter, the axion wind provides a velocity $\mathbf{v}_{\text{DM}} \sim 10^{-3}c$, which induces an effective magnetic field

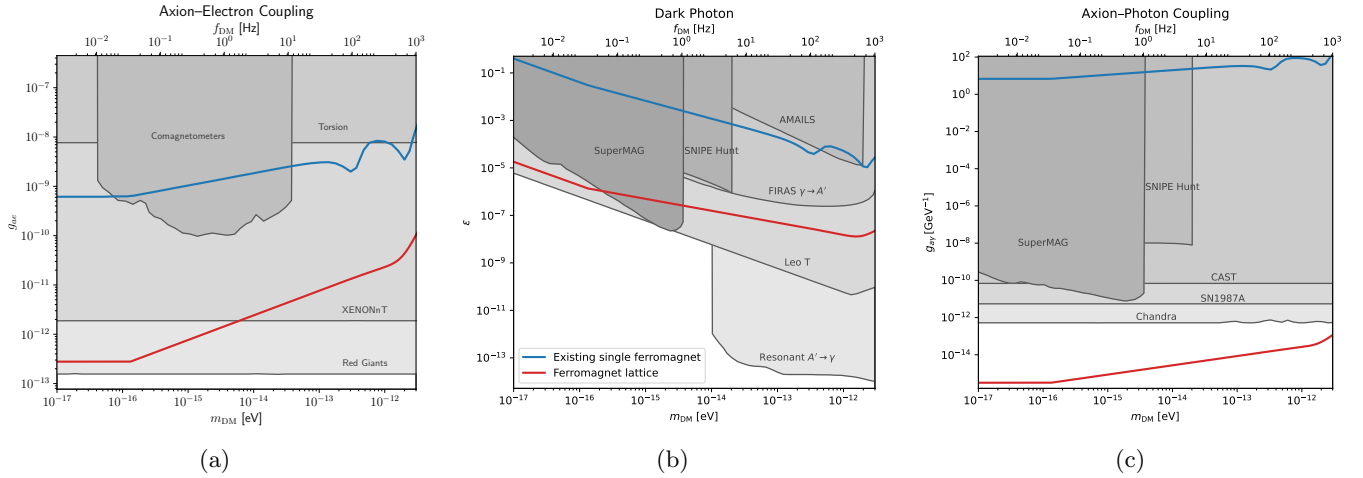


FIG. 2. Projected sensitivity to ultralight dark matter couplings as a function of the dark matter mass m_{DM} , derived from the projected noise of the proposed ferromagnet lattice magnetometer. The solid red curve shows the constraints obtained from this work. Shaded regions indicate existing constraints from the literature [15, 16]. The blue curve denotes the existing experimental constraints from a single ferromagnet magnetometer [8]. In our calculations, we take the size of the shield as $L = 1$ m, and use the same parameter setups as the existing single ferromagnet.

oscillating with frequency ω_{DM} , reading

$$\mathbf{B}_{ae} = \frac{g_{ae}}{\gamma_e m_e} \mathbf{v}_{\text{DM}} \sqrt{2\rho_{\text{DM}}} \sin(\omega_{\text{DM}} t). \quad (10)$$

The constraint on the axion-electron coupling constant is shown in FIG. 2(a).

Next, we consider dark photon dark matter, characterized by a massive vector field A'_μ kinetically mixed with the standard model photon through

$$\mathcal{L}_{A'} = -\epsilon m_{A'}^2 A'_\mu A'^\mu. \quad (11)$$

The background dark photon field generates an effective current

$$J_{\text{eff}}^\mu = \epsilon m_{A'}^2 A'^\mu, \quad (12)$$

which oscillates at its Compton frequency. The corresponding effective magnetic field is solved under the boundary condition of the magnetic shield, giving

$$B_{A'} \sim \epsilon \sqrt{2\rho_{\text{DM}}} m_{A'} L, \quad (13)$$

where L is the characteristic length of the shield. The corresponding constraint is shown in FIG. 2(b).

Finally, we consider the axion coupling to standard model photons,

$$\mathcal{L}_{a\gamma} = -\frac{1}{4} g_{a\gamma} a F_{\mu\nu} \tilde{F}^{\mu\nu}, \quad (14)$$

where $g_{a\gamma}$ denotes the axion-photon coupling constant. In the presence of a background electromagnetic field, the axion field induces an oscillatory electromagnetic response that can be described by an effective current

$$J_{\text{eff}}^\mu = g_{a\gamma} \partial_\nu a \tilde{F}^{\mu\nu}. \quad (15)$$

This mechanism underlies resonant axion searches in shielded or cavity environments [17–19], where the axion-induced current stimulates electromagnetic modes determined by the boundary conditions of the apparatus. A crucial distinction from the axion-electron and dark-photon cases considered above is that the induced signal depends linearly on the ambient electromagnetic field. The experimental configuration therefore participates directly in the signal-generation process rather than acting as a passive probe. In our setup, the dominant background field is generated by the ferromagnets themselves. The magnetic shield imposes boundary conditions that define a discrete set of cavity modes, as analyzed in detail in ref. [20]. Since both the lattice size and the minimum distance to the shield are much smaller than the characteristic shield dimension L , all ferromagnets couple identically to these low-frequency modes. These modes therefore mediate a collective electromagnetic response, in which the contributions from individual ferromagnets add coherently. Because the axion-induced signal is dominated by these low-frequency cavity modes, the resulting magnetic-like field experienced by the ferromagnets scales linearly with the number of ferromagnets, reading

$$B_{a\gamma} \sim N B_{a\gamma}^{(1)} = \mathcal{O}(0.1) N g_{a\gamma} \sqrt{2\rho_{\text{DM}}} \frac{\mu}{L^2}, \quad (16)$$

where the single-ferromagnet estimate follows refs. [8, 20]. The numerical prefactor depends on the detailed cavity geometry but remains $\mathcal{O}(0.1)$ for generic shield configurations.

This linear enhancement is qualitatively different from the scaling obtained for axion-electron or dark-photon couplings, where collective operation improves only the effective sensitivity through signal averaging. In the

axion-photon channel, the ferromagnet lattice enhances the signal generation mechanism itself, leading to a genuinely nontrivial amplification of the axion-induced magnetic response. The resulting projected sensitivity is shown in FIG. 2(c).

In conclusion, we propose and analyze a ferromagnet lattice magnetometer as a new platform for ultrasensitive detection of weak effective magnetic fields induced by ULDM. By replacing a single ferromagnet with a lattice of identical ferromagnets, the total polarized spin is increased, thereby amplifying the signal strength without introducing dynamical complications associated with scaling up a single ferromagnet. We have shown that magnetic dipole-dipole interactions, which would otherwise lead to rapid dephasing, can be dynamically suppressed through a high-frequency modulation, enabling the lattice to operate as an effectively noninteracting ensemble on magnetometry timescales. We perform a detailed analysis of the noise properties of the driven lattice and demonstrate how each noise component scales with the number of ferromagnets. Although backaction noise remains correlated across the lattice, we show that its impact can be mitigated through appropriate tuning of the pickup-coil coupling, allowing the total noise to be rebalanced near the thermal noise floor. As a result, compared to existing single ferromagnetic implementations, the lattice configuration achieves N times higher effective sensitivity. We interpret the projected sensitivity in the context of ULDM searches, focusing on axion-electron, dark photon, and axion-photon couplings. While collective operation improves sensitivity in all cases, we find that the axion-photon channel exhibits a qualitatively distinct enhancement, as the electromagnetic background generated by the lattice itself coherently amplifies the axion-induced signal. This nontrivial lattice-induced enhancement enables sensitivities that are competitive with, and in parts surpass, existing constraints. Our results establish the ferromagnet lattice magnetometer as a promising platform for future searches for ultralight dark matter, with clear pathways for further improvement through advances in SQUID noise and experimental implementation.

Acknowledgments—This work is supported by the National Natural Science Foundation of China (Grant No. 62505007).

* scx@pku.edu.cn

† james@pku.edu.cn

- [1] David J. E. Marsh, *Phys. Rep.* **643**, 1 (2016).
- [2] D. Antypas *et al.*, *New Horizons: Scalar and Vector Ultralight Dark Matter* (2022), arXiv:2203.14915 [hep-ex].
- [3] D. F. Jackson Kimball and K. Van Bibber, eds., *The Search for Ultralight Bosonic Dark Matter* (Springer International Publishing, Cham, 2023).
- [4] L. Cong, W. Ji, P. Fadeev, F. Ficek, M. Jiang, V. V. Flambaum, H. Guan, D. F. Jackson Kimball, M. G. Kozlov, Y. V. Stadnik, and D. Budker, *Rev. Mod. Phys.* **97**, 025005 (2025).
- [5] P. Fadeev, C. Timberlake, T. Wang, A. Vinante, Y. B. Band, D. Budker, A. O. Sushkov, H. Ulbricht, and D. F. Jackson Kimball, *Quantum Sci. Technol.* **6**, 024006 (2021).
- [6] S. Afach *et al.*, *Nat. Phys.* **17**, 1396 (2021).
- [7] F. Ahrens, W. Ji, D. Budker, C. Timberlake, H. Ulbricht, and A. Vinante, *Phys. Rev. Lett.* **134**, 110801 (2025).
- [8] S. Kalia, D. Budker, D. F. J. Kimball, W. Ji, Z. Liu, A. O. Sushkov, C. Timberlake, H. Ulbricht, A. Vinante, and T. Wang, *Phys. Rev. D* **110**, 115029 (2024).
- [9] A. Vinante, C. Timberlake, and H. Ulbricht, *Entropy* (Basel) **24**, 1642 (2022).
- [10] A. Marzo, S. A. Seah, B. W. Drinkwater, D. R. Sahoo, B. Long, and S. Subramanian, *Nat. Commun.* **6**, 8661 (2015).
- [11] X. Chen, K. H. Lam, R. Chen, Z. Chen, X. Qian, J. Zhang, P. Yu, and Q. Zhou, *Appl. Phys. Lett.* **114**, 054103 (2019).
- [12] D. Foresti, M. Nabavi, M. Klingauf, A. Ferrari, and D. Poulakakos, *Proc. Natl. Acad. Sci. USA* **110**, 12549 (2013).
- [13] Y.-H. Tseng, *PRX Quantum* **6**, 10.1103/j76m-gcp1 (2025).
- [14] A. A. Clerk, M. H. Devoret, S. M. Girvin, F. Marquardt, and R. J. Schoelkopf, *Rev. Mod. Phys.* **82**, 1155 (2010).
- [15] A. Caputo, A. J. Millar, C. A. J. O’Hare, and E. Vitagliano, *Phys. Rev. D* **104**, 095029 (2021).
- [16] C. O’Hare, cajohare/axionlimits: Axionlimits, <https://cajohare.github.io/AxionLimits/> (2020).
- [17] S. Chaudhuri, P. W. Graham, K. Irwin, J. Mardon, S. Rajendran, and Y. Zhao, *Phys. Rev. D* **92**, 075012 (2015).
- [18] J. L. Ouellet, C. P. Salemi, J. W. Foster, R. Henning, Z. Bogorad, J. M. Conrad, J. A. Formaggio, Y. Kahn, J. Minervini, A. Radovinsky, *et al.*, *Phys. Rev. Lett.* **122**, 121802 (2019).
- [19] S. J. Asztalos, G. Carosi, C. Hagmann, D. Kinion, K. van Bibber, M. Hotz, L. J. Rosenberg, G. Rybka, J. Hoskins, J. Hwang, *et al.*, *Phys. Rev. Lett.* **104**, 041301 (2010).
- [20] G. Higgins, S. Kalia, and Z. Liu, *Phys. Rev. D* **109**, 055024 (2024).